Chapter 1

Landslides Caused by Climate Change and Groundwater Movement in Permafrost Mountain

Wei Shan, Ying Guo, Zhaoguang Hu,
Chunjiao Wang and Chengcheng Zhang

Additional information is available at the end of the chapter

http://dx.doi.org/10.5772/63068

Abstract

Climate change induced warming results in permafrost degradation. Melting permafrost subsequently leads to an increased incidence of landslides. The study area was within the northwest section of the Lesser Khingan Range in northern China along the Bei'an-Heihe Highway. We analyzed the impact of climate change on landslide movement in the permafrost zone via a combination of geological survey and meteorological data. The average annual temperature of the study area has increased by 3.2°C in last 60 years, and permafrost degradation is severe. Loose soil on the hillside surface provides appropriate conditions for the infiltration of atmospheric precipitation and snowmelt, and seepage from thawing permafrost. As it infiltrates downwards, water is blocked by the underlying permafrost or dense soil, and infiltrates along this barrier layer toward lower positions, forming a potential sliding zone. The combination of high density resistivity (HDR) methods based on soil resistivity values, ground-penetrating radar (GPR) methods based on characteristics of radar wave reflection, respectively, and geological drilling can be utilized to determine the regional stratigraphic distribution. This will allow the exact location of the landslide sliding surface to be precisely determined. Field test results indicate that radar reflectivity characteristics and the resistivity values of the soil in the landslide mass is significantly different from surrounding soil. There are sudden decreases in the apparent resistivity values at the sliding surface location. In addition, the radar exhibits strong reflection at the sliding surface position, with a sudden increase in the amplitude of the radar wave. Drilling results indicate that the soil has high water content at the location of the sliding surface of the landslide mass in the study area, which is entirely consistent with the GPR and HDR results. Thus, abnormal radar wave reflection and abrupt changes in apparent resistivity values can be used in practice to identify the location of landslide sliding surfaces in this region. We produce a detailed analysis of a representative landslide within the study area. Displacement monitoring locations were positioned at the trailing edge of the landslide mass and on the landslide mass surface.

We then used this data to determine the relationships of landslide movement with both ground temperature and the trailing edge pore water pressure. The results suggest seasonal variation in the landslide movement process and characteristics of an annual cyclical trend. Landslide movement can be described by intermittence and low angles. The slip rate and the timing of slide occurrence exhibit relationships with the trailing edge pore water pressure of the landslide mass. The seepage of thaw water into the landslide mass will impact the trailing edge pore water pressure of the landslide mass. This phenomenon is identified as the primary cause of landslide movement.

Keywords: climate change, groundwater movement, permafrost, landslides, mountains

1. Introduction

The area north of 47° N in northeast China exhibits widespread permafrost. This represents the sole high-latitude permafrost region in China. This region also represents the second largest permafrost region in China [1–3]. In recent years, the southern boundary of this high-latitude permafrost region has gradually moved to the north as a result of climate change. Permafrost proximate to the southern boundary exhibits accelerated degradation and a distribution that is discontinuous and island-like [4–6].

Climate change refers to the temporal alteration of the baseline state of climate. The mean global surface temperature has been increasing throughout the last century. The rate of warming during 1957–2007 was almost double the rate during 1957–2007 [7]. Temperatures in a majority of the permafrost regions throughout the world have risen since the early 1980s. The recorded temperature rise has reached 3°C in some regions in northern Alaska, and the rise has reached 2°C in the northern regions of Europe and Russia. During the period of 1975–2005, there were significant reductions in the range and thickness of the permafrost layer in the northern area of Russia [8]. Climate change and its impact are an important research issue receiving extensive global attention.

A number of studies have demonstrated that climate change in China has presented the same tendency as the global trend [9]. The temperature increase rate in China for the last 54 years was approximately 0.25°C/10a. This value is far exceeds the hemispheric and global average rates of warming. Northeast China is among the national areas exhibiting the most notable warming and permafrost degradation [10].

Accumulated snow and vegetation have extremely significant impacts on the thawing process of the underlying seasonal frozen ground and permafrost [11]. Temperature shifts caused by snow, vegetation, water, topography, atmospheric inversion, and other local factors can be substantial in the Great and Lesser Khingan Ranges of northeast China and the Outer Baikal region of Russia. This results in the "Khingan–Baikal type" permafrost that differs from high-altitude and polar permafrost distributions [12, 13]. The form and process of high-latitude permafrost degradation in northeast China are also affected by the occurrence conditions. Therefore, the form and process of degradation in this region differ from their analogs in high-altitude and polar [14].

http://dx.doi.org/10.5772/63068

Landslide events tied to extreme weather and climate change have increased in recent years [15], and have gradually received attention from national governments and relevant international academic organizations [16, 17]. In particular, landslides in cold areas are becoming a hot issue in landslide research [18, 19].

Landslides are geological phenomena that naturally occur in mountainous areas. The triggering mechanism and evolution of landslides are closely tied to environmental factors and geological conditions. Landslides are influenced by geological forces, lithologic structure, and other crustal internal factors as well as by land cover, topography, human activities, precipitation, and environmental conditions. The temporal and spatial distribution of landslides exhibits characteristics of continuation, uncertainty, intermittency, and irreversibility. Landslides are the result of environmental and geological changes and their occurrence can dramatically alter the geology of an area [20]. Scientists have applied various methodologies to analyze the relationships between climate change in cold areas and landslide evolution and mechanisms [21]. These studies have discussed the landslides induced by permafrost and glacier degradation and their impact on the geology, topography, biodiversity, and water resources. Climate has also been investigated as a main factor influencing the landslide evolution in cold regions [22–28]. However, the preponderance of these studies were conducted at large-scales due to a lack of observational data [29]. To date, there have been no studies on the movement characteristics, mechanisms, and patterns of landslides caused by the combined effects of extreme weather events and permafrost thawing.

In the present study, we designate the area surrounding the intersection of the Bei'an to Heihe Highway with the northwest region of the Lesser Khingan Range as the study area. We conducted field measurements, a geological survey, and an engineering survey. These data sets were plotted on a geological cross section and a topographic map of the landslide area. We investigated the impact of climate change on geological environment, permafrost thaw, and landslide mechanisms in the study area via meteorological data from Sunwu County (30 km from the study area) provided by the China Meteorological Data Sharing Service System (http://cdc.cma.gov.cn/home). In order to conduct a comprehensive analysis of the impact of climate change on the landslide movement process and the pore water pressure, we utilized point displacement on the landslide mass, trailing edge ground temperature, and pore water pressure data sets collected from the landslide area of the Landslide K178 + 530. In addition, in this paper we apply a combination of geophysical techniques (HDR and GPR) and traditional methods (drilling and mapping) to Landslide K178 + 530 that occurred in the Lesser Khingan Range of northeast China. Landslides occur frequently in this region due to atmospheric precipitation and permafrost degradation. We aim to determine the thickness and internal structure of the study landslide and thereby ascertain the applicability of GPR and HDR for these regional types of landslide.

2. Background

The study area ranges between 127° 17′ 31″–127° 21′ 24″ east longitude and 49° 30′ 57″–49° 41′ 50″ north latitude (**Figure 1**). In this area, the northwest section of the Lesser Khingan Range

intersects the Bei'an-Heihe Highway at the border between Sunwu County and the Aihui District. The area is located on the southern fringe of China's high-latitude permafrost region and has typical periglacial landforms. The island-like permafrost in this region is the result of residual paleo-glacial deposition and is currently in the degradation stage. The geological conditions are extremely unstable.

Figure 1. High-latitude permafrost distribution in Northeast China (data from Zurich University, Switzerland), and the location of study area.

2.1. Climate conditions

The study area is positioned in the transition area between the cold-temperate zone and the northern area of the middle temperate zone. The area is subject to monsoons as well as alternating influences from high and low pressures originating from inland and the ocean. Generally, the study area experiences dry, cold, and long winters as well as hot, humid, and short summers. It is classified as a continental monsoon climate zone.

In the study area, the average annual temperature is within the range of −2 to 1°C, with an extreme minimum of −48.1°C and an extreme maximum of 38.6°C. The average annual precipitation is within the range of 530–552 mm, with a maximum of 800 mm. Precipitation is mostly concentrated from July to September during the summer. The precipitation that falls during this period accounts for 61–67% of the total yearly precipitation. The first snow fall is typically in mid-October, and the final snow fall is often in late March or early April of the following year. The annual average wind speed is 2.7–4.0 m/s. The minimum annual evaporation is 850 mm and the maximum annual evaporation exceeds 1000 mm. The average annual total radiation is 1148 kcal/cm^2, with a minimum of 1039 kcal/cm^2 and a maximum of

http://dx.doi.org/10.5772/63068

1229 kcal/cm^2. The average annual sunshine is 2500 h, with a minimum of 2200 h and a maximum of 2800 h.

2.2. Permafrost distribution

The climate in Northeast China is subject to the Siberia-Mongolia high-pressure system. This region has a widely distributed inversion layer. This layer has important impacts on the regional distribution and development process of permafrost. Meanwhile, the majority of forest area in China is distributed in the northeast region. In this area, permafrost coexists and is influenced by wetlands, grasslands, and forests. Forests, mosses, shrubs, and other ground covers reduce absorption of solar radiation, thereby decreasing ground and air temperatures. The valleys, low-lying river terraces, shady slopes, and wetlands provide suitable conditions for slow permafrost degradation as well as the development of island-like permafrost.

In the study area, the seasonal frozen ground reaches its maximum depth at the end of May. The recorded maximum depth of seasonal frozen ground is in the range of 2.26–2.67 m. In the mountains, the maximum depth of seasonal frozen ground can exceed this range. The thawing period of seasonal frost is April to September. All the seasonal frost in dry areas thaws by early July. However, seasonal frosts do not completely thaw in swampy areas with thick peat and humus zones until the end of October. Island-like permafrost is mainly distributed in valley areas and on shaded slopes.

2.3. Climate change in the study area

Due to global climate change, the study area is among the regions in northeast China that have experienced the largest temperature increases during the past 50 years. Sunwu County meteorological data indicate that during the past 60 years, change in temperature was the most significant among all climate indicators. Using meteorological data from Sunwu County,

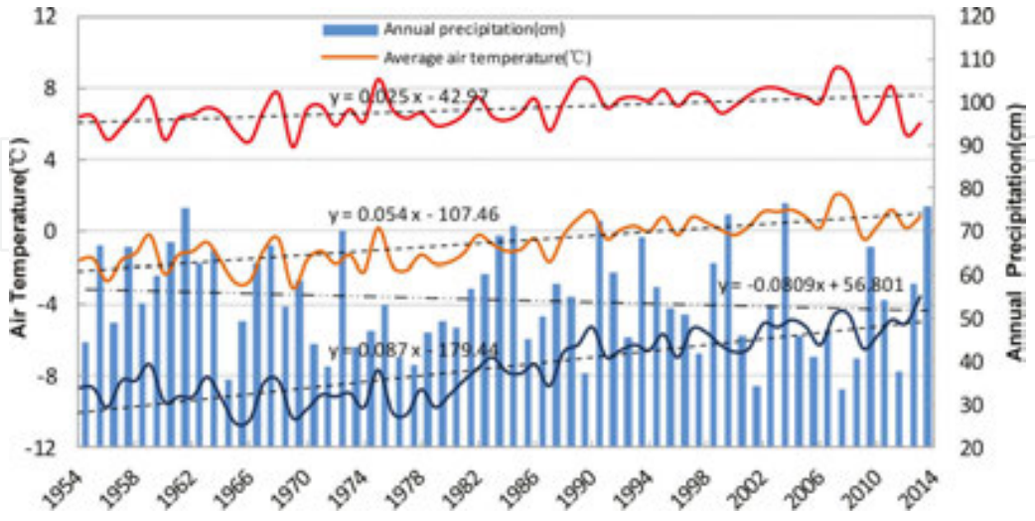

Figure 2. Annual average maximum temperatures, average temperatures, average minimum temperatures and average precipitation in Sunwu County (1954–2013).

Figure 2 shows the yearly average temperatures, average maximum temperatures, average minimum temperatures, and average precipitation from 1954 to 2013. Linear regression indicates that during the 60 year period from 1954 to 2013 the annual average temperature increased by 3.2°C; the average annual minimum temperature increased by 5.2°C (69.04%); the average annual maximum temperature rose by 1.5°C (21.99%); and the average annual precipitation decreased by 4.85 cm (8.93%). The average annual minimum temperature increase was 3.45 times the increase in the average annual maximum temperature.

The permafrost distribution map generated from the Enhanced Thematic Mapper (ETM+) data collected in 2009 via the Landsat7 satellite (**Figure 3**) indicates that the landslide locations match the permafrost distribution to a high degree [30]. We therefore conjectured that these landslides were the result of thawing permafrost.

Figure 3. Permafrost distribution map in K176 + 500–K180 + 000 section of Bei'an-Heihe Highway.

2.4. Climate change and landslides

Climate change in the study area has led to permafrost degradation, and engineering projects have exacerbated the permafrost degradation process [31]. In 1999, a planning survey conducted for the secondary road from Bei'an to Heihe indicated that along the entire road length there were 17 permafrost road segments [32, 33]. However, a survey conducted right before the construction of the Bei'an-Heihe Highway in 2009 showed that there were only six permafrost road segments remaining; the other 11 segments had been completely degraded.

The survey conducted in 2009 showed that within 10 m of the left of the roadbed in the K177 + 400 to K179 + 200 section there were four landslides with a total volume that exceeded 20,000 m^3 (**Figure 6**). In addition, there were numerous landslides within 3 km of this road section (**Figure 4**).

http://dx.doi.org/10.5772/63068

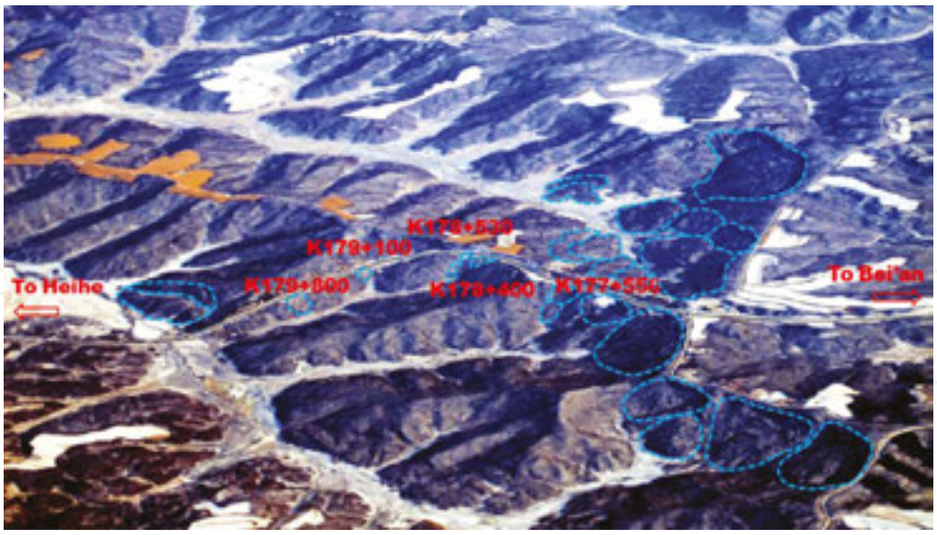

Figure 4. Full view of K175 + 500–K180 + 200 section of Bei'an-Heihe Highway (blue line is the boundary of the landslides, the orange area is corn field).

Figure 5. Satellite photos of K176 + 500–K179 + 900 section of Bei'an-Heihe Highway (Google earth). (A) Landslide in K178 + 530 section (in 2000); (B) satellite photos of K178 + 530 (2004.6); and (C) satellite photos of K178 + 530 (2010.9).

The phase change of water during the thawing of permafrost has a significant impact on the soil's mechanical properties [34]. Permafrost degradation causes a multitude of geological engineering issues for road construction. In 1999, the Bei'an-Heihe secondary road construction began. A landslide was caused by thawing of permafrost in the roadbed during August 2000 in the K176 + 900 to 178 + 200 section. This necessitated the abandonment of this section due to instability over the entire roadbed. The road had to be redirected along the left side of the ridge (**Figure 5A**).

2.5. Topography and geological structure

The study area encompasses a hilly landscape with rolling terrain. The slope is typically within the range of 10–20°. The upper sections of the slopes are usually within the range of 25–30° but can reach up to 40°. The area can also be divided into hills and valley bottomland. The altitude range over the entire area is 210–330 m. A 2010 survey also showed that, in the section between K177 + 400 and K179 + 200, there were four landslides within 10 m of the left of the roadbed with a total surface area of over 2000 m^2 (**Figure 6**). The four landslides are located at the A, B, C and D position, respectively. C illustrates Landslide K178 + 530. **Figure 6** shows the geologic and geomorphic map of the landside road area of the study area plotted from the field survey conducted in June 2010.

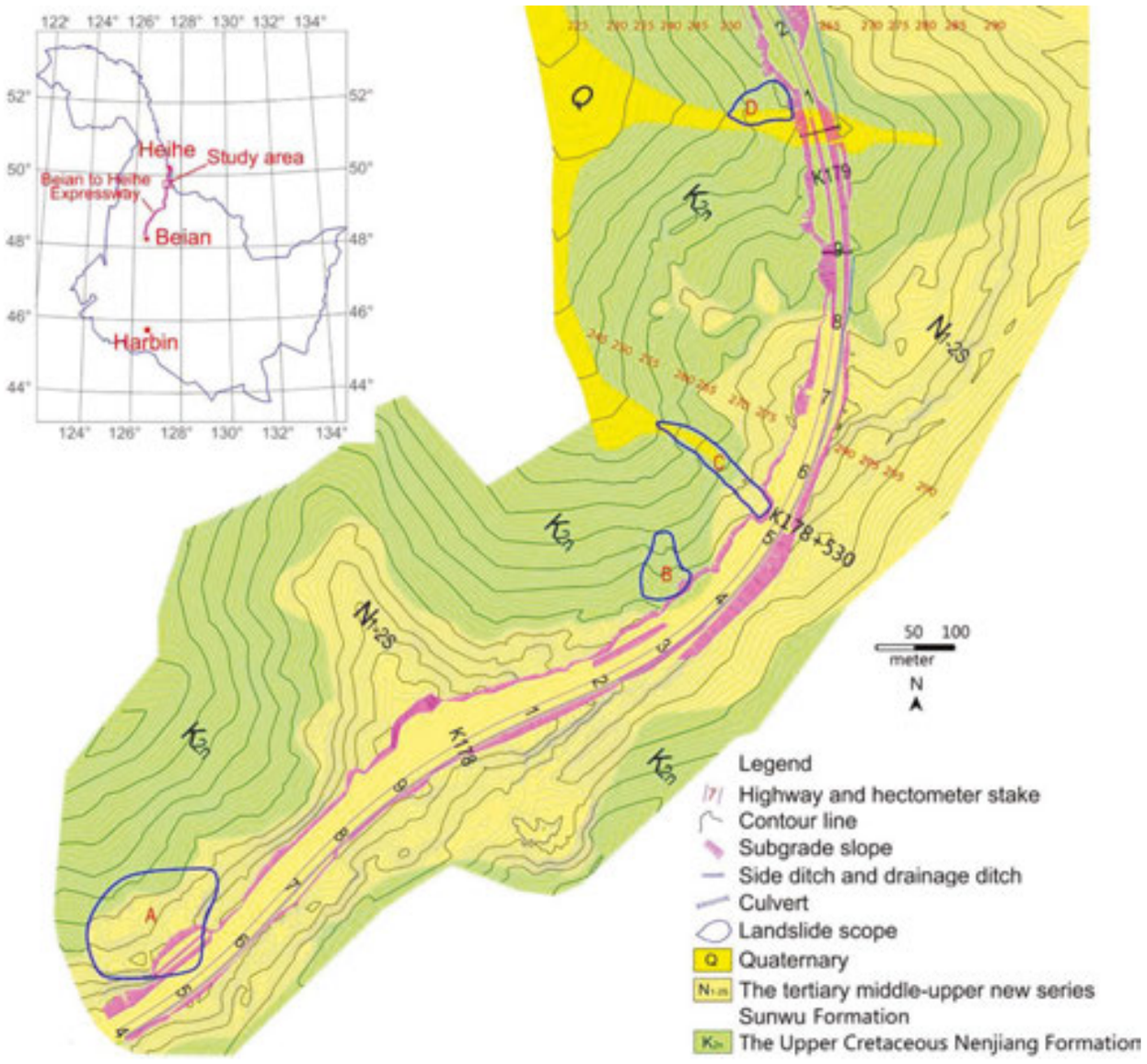

Figure 6. Geological map of K177 + 400–K179 + 200 section of Bei'an-Heihe Highway.

http://dx.doi.org/10.5772/63068

The geology of the study area can be characterized as belonging to the Khingan-Haixi fold belt. Beginning at the surface and moving down, the stratigraphy is composed of powdery sandstone, silty mudstone, Tertiary pebbly sandstone, and Cretaceous mudstone. The Lesser Khingan Range experienced block uplift during a period from the late Tertiary to the early Quaternary. Due to leveling and long-term erosion, loose sediment has gradually thinned at the summit and on the slopes of hills. The current residual layer is typically only 1–2 m thick. The loose deposits mainly accumulate with a thickness of approximately 10 m in the valley and basin areas between mountains. The soil is mainly composed of mild clay, clayey silt, and gravelly sand. The ground is covered with a relatively thick layer of turf and grass peat. The surface vegetation is composed of woodland and grassland, and there are inverted trees in the woodlands.

Landslide K178 + 530 is positioned at the widened embankment on the left side of the Bei'an-Heihe Highway (**Figure 7**). The surface soil and the roadbed soil slide together along the valley, and the maximum slippage is 200 m distance from the road. This landslide mass is 20–30 m wide and covers an area of approximately 6000 m^2. The distance between the leading and trailing edges is 200 m. The height of the trailing edge is 285 m, and the height of the leading edge is 254 m. The landslide trailing edge has an arc-shaped dislocation that is positioned within the widened embankment.

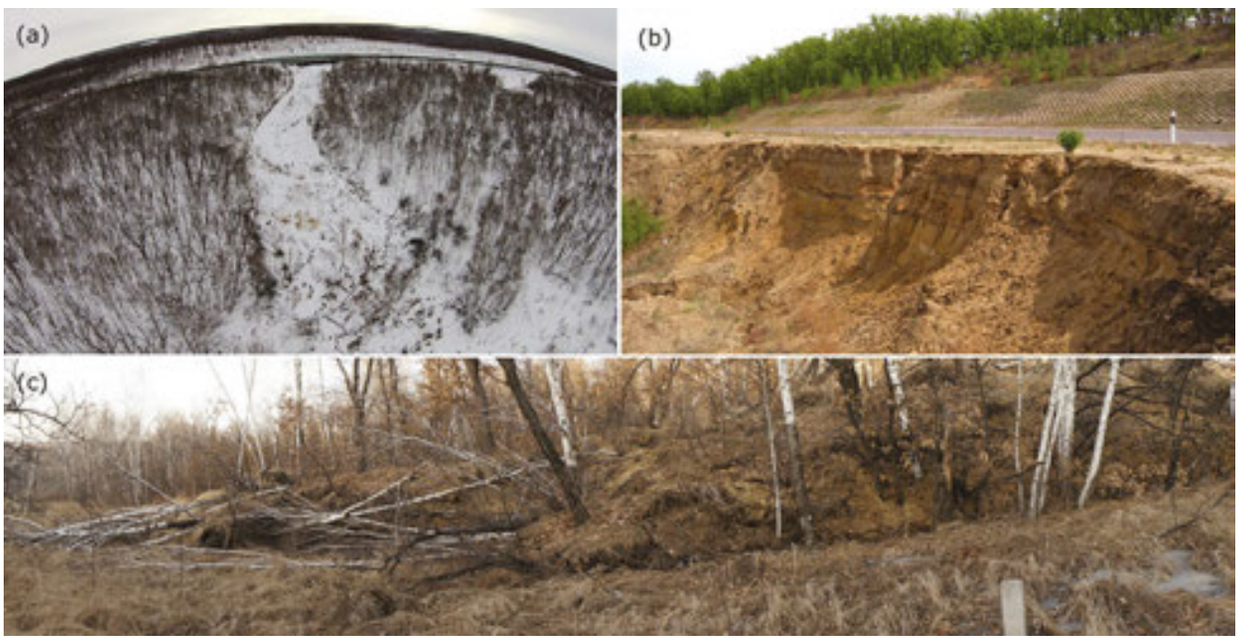

Figure 7. Landslide scene photos: (a) Panoramic view of landslide (in November 2014); (b) the trailing edge of landslide (in June 2010); and (c) the leading edge of landslide (in October 2013).

For prospecting purposes, four boreholes were drilled into the K178 + 530 section. The borehole depths were within the range of 14–26 m, and the distribution of boreholes is presented in **Figure 8**. The drilling revealed the soil profile as follows, from bottom to top: Cretaceous mudstones, siltstones, Tertiary pebbly sandstones, and Quaternary loose Embankment:

yellow, primarily composed of loosely mixed Tertiary pebbly sandstones, sandy mudstones, and Cretaceous mudstones; the soil is plastic when saturated with water and loose when dry. Clay: yellow, plastic and with high rigidity and strength when dry. The downstream region of the landslide mass has a depth distribution within the range of 0–6.7 m. The upstream region of the landslide mass has a depth distribution within the range of 1.5–3.8 m. There are numerous sandwiched grit layers, and one of these layers is approximately 1–10 cm thick. These layers greatly enhance the soil water seepage capacity.

Tertiary pebbly sandstones: distributed in the embankment within the range of 2.0–3.4 m depth. The upstream region of the landslide mass is within the range of 3.8–4.5 m depth. This area is mainly composed of weathered feldspar stone and mineral sands that are well-graded with high permeability. Fully weathered siltstones: yellow, distributed in the upstream region of the landslide mass at a depth of 4.5–9.7 m, sandy, of bedding structure and poor water seepage capacity.

Fully weathered mudstone: yellow or gray-green and pelite. They exhibit a layered structure and poor water seepage capacity. They are easily softened by water. Strongly weathered mudstones: dark gray, pelite, of layered structure, weakly cemented rock. Moderately weathered mudstones: brown, black and gray, pelite, layered structure.

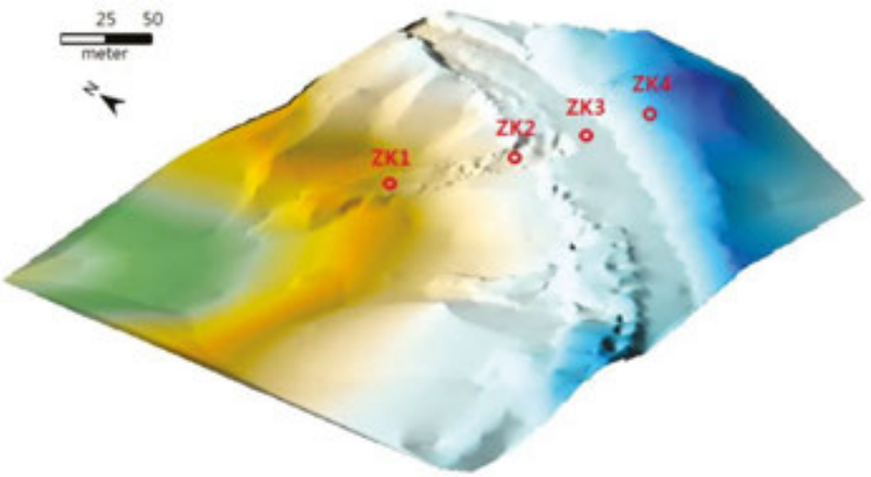

Figure 8. Drilling borehole layout on Landslide K178 + 530 and the geomorphological map of the landslide area (using SURFER software to draw the geomorphological map based on GPS terrain data in June 2010).

3. Geophysical research methods

In this paper we present combination geophysical techniques of HDR and GPR on the landslide K178 + 530 on the Bei'an-Heihe Highway in Lesser Khingan Range of northeast China. The survey lines were established, as shown in **Figure 9**.

http://dx.doi.org/10.5772/63068

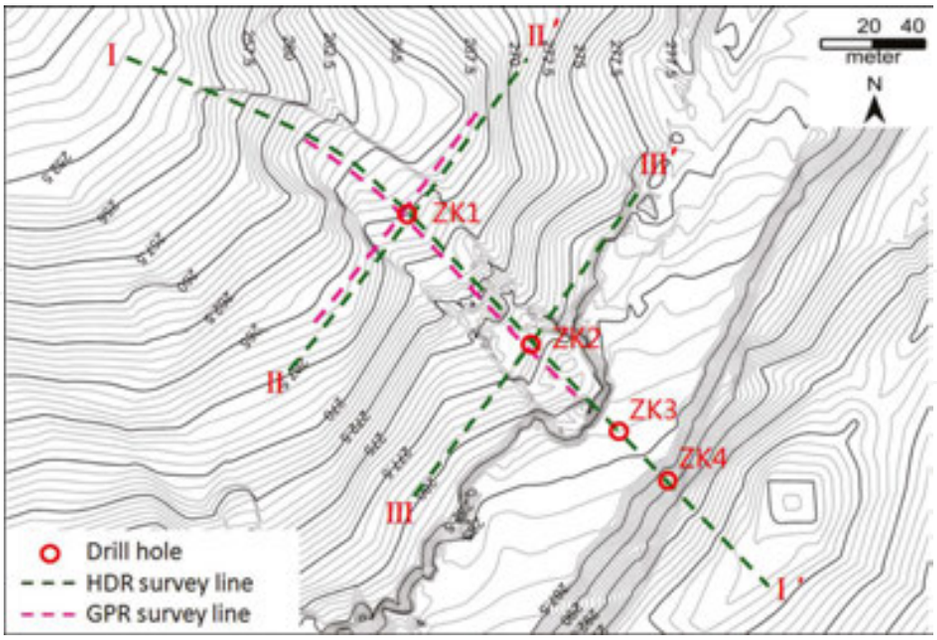

Figure 9. The layout of the Landslide K178 + 53 geophysical survey lines. (1) HDR survey lines. A total of three HDR survey lines, i.e., I–I′, II–II′ and III–III′, were established on the Landslide K178 + 530 road section. Line I–I′ passed through the center of the landslide mass and was oriented along the sliding direction. The survey line start point was 40 m from the leading edge of the landslide mass. The survey line passed the drilling boreholes ZK1, ZK2, ZK3 and ZK4 in sequence. The survey line has a total length of 357 m (300 m horizontal distance). Line II–II′ was oriented to be perpendicular to the sliding direction and began 110 m away from the trailing edge. Point ZK1 was the midpoint of this line with a total length of 177 m. Along this line, 1–60 numbered electrodes were arranged in order from left to right. Line III–III′ was also oriented perpendicular to the sliding direction but was had a start position 50 m away from the trailing edge. Point ZK2 served as the midpoint of this transect with a total length of this survey 177 m. A similar set up of electrodes was also deployed in this transect. The data collection date is September 3, 2012. (2) GPR survey lines: we set up two survey lines with the locations that corresponded to the HDR survey lines. However, the start and end points were different. The HDR survey lines were longer than the GPR survey lines. The two survey lines (I–I′ and II–II′) had lengths of 150 m and 118 m, respectively. The data collection date is October 1, 2013.

3.1. HDR method

The WGMD-9 Super HDR system produced by the Chongqing Benteng Digital Control Technical Institute (Chongqing, China) was utilized in this study. Within this system, the WDA-1 super digital direct current electric device is used for control host and measurement. Centralized two-dimensional HDR measurements can be generated via the optional WDZJ-4 multi-channel electrode converter, electrodes, and centralized high-density cables. The RES2DINV software was used to perform the inversion of the apparent resistivity data sets. This software package generates a two-dimensional model of the subsurface via apparent resistivity pseudo-sections [35]. A Wenner configuration was employed to acquire the relevant data. The method utilizes the inversion of pseudo-section data via smoothness-constrained least squares [35–37]. The subsurface in this algorithm is subdivided into rectangular blocks with constant resistivity. The resistivity of each block is then assessed via an iterative scheme that minimizes the difference between calculated and observed pseudo-sections using an iterative scheme. The smoothness-constraint leads to results with smooth resistivity changes.

The derived pseudo-sections can be generated either via finite-element or finite-difference methods [38, 39]. In this study, we employed the finite element scheme due to the changes in the study area topography.

We utilized the smoothness-constraint least squares method in the inversion model. Fundamentally, this method is used to constantly adjust the model resistivity through model correction to reduce the difference between the calculated apparent resistivity and the measured resistivity, and to describe the degree of fit between the two using the mean square error. The smoothness-constraint least squares method, which has been widely applied, has a number of advantages, such as adaptability to different types of data and models, relatively small noise influence on the inversion data, rapid inversion, high sensitivity to deep units, and a small number of iterations. In tests utilizing the HDR method, the maximum exploration depth of the survey lines was determined to be 30 m and the spacing between unit electrodes was 3.0 m.

We established three HDR survey lines on the Landslide K178 + 530 road section, i.e., I–I′, II–II′ and III–III′ (**Figure 9**). The date of data collection is September 3, 2012.

3.2. GPR method

The GPR instrument used was the RIS-K2 FastWave Ground Penetrating Radar produced by IDS Corporation (Italy). We utilized an unshielded dual radar antenna that operated at low-frequency 40 MHz. The time window of detection was set at 600 ns, the sampling rate was set at 1024, and a 0.05 m data acquisition track pitch was employed. Two GPR survey lines were set up (**Figure 9**) with orientations that coincided with the HDR survey lines, but termination points of the GPR survey lines were different. The two survey lines (I–I′and II–II′) had lengths of 150 m and 118 m, respectively. The date of data collection is October 1, 2013. Raw GPR data were processed via the REFLEXW software produced by Sandmeier Scientific Software (Karlsruhe, Germany). The coordinates of each trace were calculated at equal distances. The surface signal reflection was set to time zero. Noise and low frequency parts of the spectrum were filtered by applying bandpass and dewow methods. In the following step of processing, we eliminated temporally consistent signals via a background removal technique. Topographical correction was then performed. The picks were exported along with the two-way travel time attribute. The propagation velocity of the wave in this case appears to be approximately 0.10 m/ns.

4. Results, analysis, and discussion of HDR

4.1. Survey line I–I′

The apparent electrical resistivity profile data for line I–I′ as collected on September 3, 2012 is presented in **Figure 10**. The figure clearly shows distinct layering in the soil resistivity values of the landslide mass. The RES2DINV software is able to extract the resistivity curve value for any transect point. This allows further analysis of the relationship between soil resistivity

http://dx.doi.org/10.5772/63068

changes and depth. **Figure 11** presents the curves of soil resistivity vs. depth at boreholes ZK1 and ZK2.

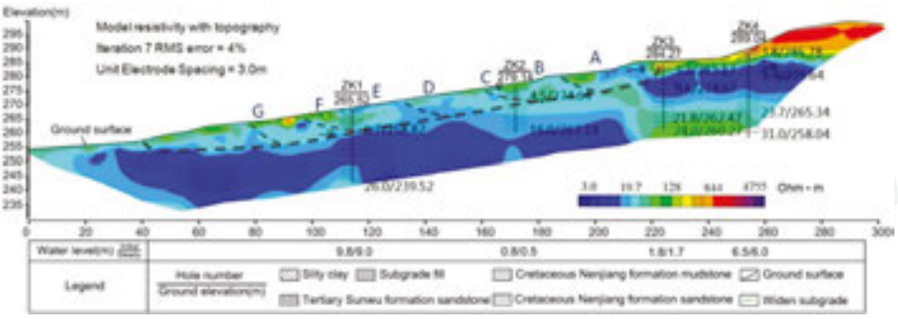

Figure 10. Comparison of drilling results and electrical resistivity profile of the survey line I–I′. Geological drilling date is in June 2010, HDR detection date is on September 3, 2012. The dashed thick black line indicates the position of the major sliding surface, and the dashed thin black lines illustrate the secondary sliding surfaces.

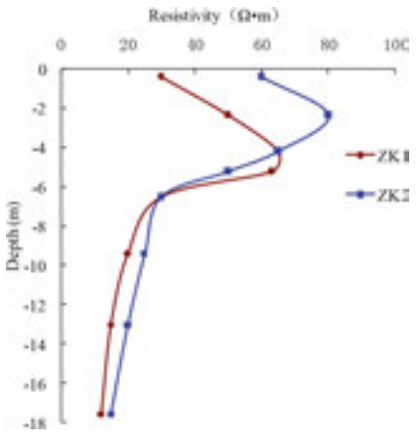

Figure 11. The electrical resistivity curves at positions ZK1 and ZK2.

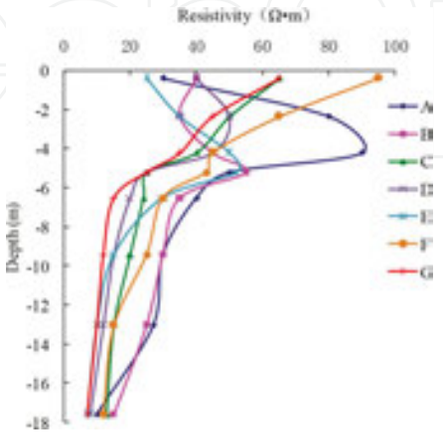

Figure 12. The electrical resistivity curves at different points on the survey line I–I′.

The ZK1 borehole is located 115 m from the beginning point of the HDR survey line. At a depth of 0–2.1 m, the soil is rather loose silty clay and is composed of approximately 15% grass roots and other organic matter. The resistivity values at this depth are in the range of 25–45 Ohm m. At the 2.1–6.7 m depth, the soil is primarily silty clay with localized weathered sand layers. The resistivity values for this depth are within the range of 45–65 Ohm m. Within the range of 6.7–8.0 m depth, the soil is composed of yellow mudstone. It is difficult for the water to infiltrate downward as the permeability coefficient is small. This forms a layer where water easily gathers. There are relatively low resistivity values in this layer, i.e., 20–30 Ohm m. At a depth of 8.0–26 m, the soil is gray mudstone, close to or below the water table. The resistivity value is relatively low, i.e., 10–25 Ohm m. As shown in the curve, silty clay contacts mudstone at a depth of 6.7 m, and resistivity exhibits apparent layering, the resistivity value decreased suddenly.

The ZK2 borehole is located 175 m from the beginning point of the survey line. At depths in the range of 0–4.5 m, the soil is somewhat loose. The resistivity values in this layer are within the range of 45–80 Ohm m. The surface embankment soil is dominated by silty clay (depth 0–3.8 m) and gravelly sand (depth 3.8–4.5 m) with resistivity values within the range of 60–80 Ohm m and 45–60 Ohm m, respectively. At the 4.5–9.7 m depth range, the soil is siltstone and primarily composed of relatively small particles. This layer exhibits poor permeability, forming a watertight layer where water can easily gather. The resistivity values are within the range of 25–35 Ohm m. At the 9.7–14.6 m depth range, the soil is composed of sandstone, and the resistivity values are within the range of 15–25 Ohm m. As the gravelly sand contacts the siltstone at a depth of 4.5 m, the resistivity value decreases suddenly.

The RES2DINV software was used to generate the soil resistivity curves along survey line I–I′ at points A, B, C, D, E, F and G (**Figure 10**). The horizontal distances between the starting point and the points A, B, C, D, E, F and G of line I–I′ are 80 m, 100 m, 120 m, 140 m, 160 m, 180 m and 200 m, respectively. The obtained soil resistivity curves are shown in **Figure 12**. At position A, the soil resistivity value decreased abruptly at a depth of 4.5 m. In other words, the soil resistivity values exhibited abrupt stratification at this depth. It can thus be determined that the sliding surface is located at a depth of 4.5 m. Similarly, the depths of the sliding surface at points B, C, D, E, F and G on line I–I′ were determined to be 5 m, 4.7 m, 5.5 m, 6.5 m, 6 m, and 5.5 m, respectively.

The above resistivity curves and HDR profiles illustrate that the soil resistivity values are clearly different and exhibit an abrupt stratification above and below the sliding surface of the landslide mass. The locations of the major sliding surfaces along the line I–I′ were deduced according to this typical sliding surface characteristic. These are illustrated with the thick dashed black line in **Figure 10**. The sliding power originated from the trailing edge of the landslide and the sliding type was propelled sliding. The minimum slip rate occurred at the leading edge. The maximum slip rate was at the trailing edge, followed by the intermediate portion of the landslide [40]. Secondary sliding in the landslide mass occurred as a result. Combining the results of the drilling exploration as well as the changes in the soil resistivity values of different positions in the landslide mass and, the secondary sliding surface was obtained, as shown via the thin dashed black line in **Figure 10**.

http://dx.doi.org/10.5772/63068

4.2. Survey line II–II′

The apparent electrical resistivity profile measured along survey line II–II′ is presented in **Figure 13**. **Figure 14(a)** shows the soil resistivity curves of points C, D ZK1, E and F of line II–II′. The distances between points C, D ZK1, E and F and the beginning point of the survey line are 80 m, 85 m, 90 m, 95 m and 100 m, respectively. Based on **Figures 13** and **14(a)**, we can know the changes in the soil resistivity values, there are apparent resistivity layering at the depths of the sliding surfaces, the resistivity value decreased suddenly. According to this characteristic of the sliding surface, the positions of the sliding surfaces along line II–II′ were deduced, as shown by the black dotted line in **Figure 13**. Based on the changes in the soil resistivity values, it can be inferred that the depths of the sliding surfaces at positions C, D, ZK1, E and F on line II–II′ were 4 m, 6 m, 6.5 m, 5.5 m and 3.5 m, respectively. **Figure 14(b)** illustrates the soil resistivity curves at the A, B, G and H locations (all outside the landslide mass) along the II–II′ survey line. The distances between the start point of the survey line and the points A, B, G and H were 40 m, 60 m, 110 m and 130 m, respectively. As can be seen in **Figure 14(b)**, the soil resistivity values of the stable soil body outside the landslide only showed stratification in the surface loose layer. As depth increased, the resistivity basically exhibited a monotonic decline, and there was no abrupt stratification.

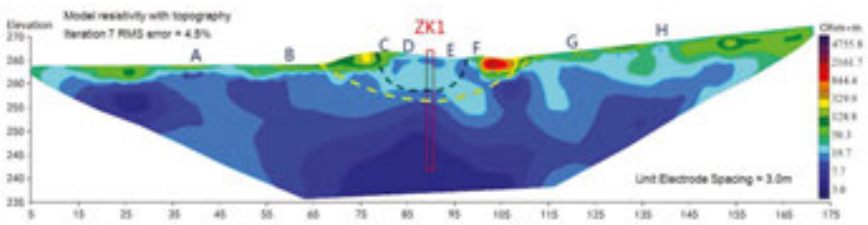

Figure 13. Survey line II–II′ electrical resistivity profile. HDR collection date of September 3, 2012. The dashed black line represents the current sliding surface. The dashed yellow line illustrates the sliding surface position of the paleo-landslide.

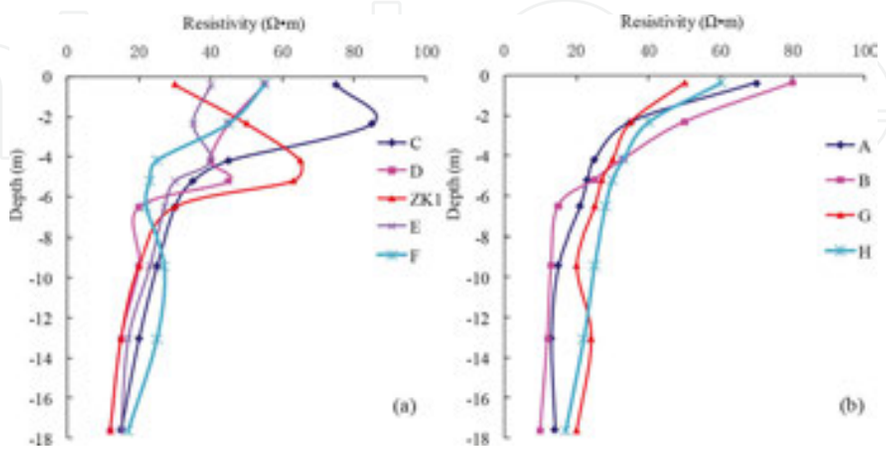

Figure 14. The electrical resistivity curves at different points on the survey line II–II′ (points C, D, ZK1, E and F are all on the landslide mass, points A, B, G and H are all outside the landslide mass).

This landslide represents a recurring landslide that has once again slipped [40]. The dashed black line in **Figure 13** illustrates the current sliding surface. By combing the geological survey at the site, and the resistivity change characteristics, we can infer the location of the sliding surface for the paleo-landslide, as illustrated by the dashed yellow line in **Figure 13**.

5. Results, analysis, and discussion of GPR

5.1. Survey line I–I′

The profile determined by the GPR survey line I–I′ is illustrated in **Figure 15** (due to the constraints under field conditions, this GPR survey line can only be used to measure this long section). The layer picking option (phase follower) of the REFLEXW software can identify a continuous reflector (the thick dashed red line in **Figure 15**). The radar-wave reflection intensity differed significantly from the reflection intensity of the surrounding medium. The strong reflected-wave signal exhibits characteristics of a distinctive horizon. The signal presents a low-frequency high-amplitude sync-phase axis. We conclude that this represents the sliding surface. The sliding surfaces exhibit good continuity and essentially reflect the landslide mass development depth range [41, 42].

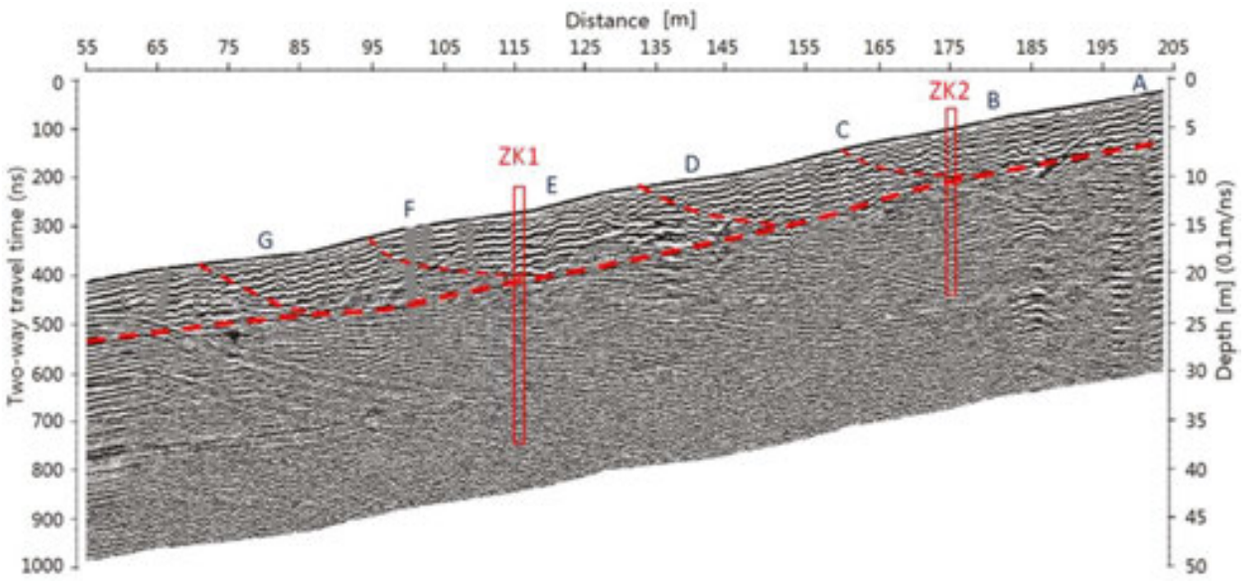

Figure 15. The GPR profile of the survey line I–I′. The radar antenna was a low-frequency 40-MHz unshielded dual antenna, the measuring date is October 1, 2013. The thick red dashed line show the position of the major sliding surface, the thin red dashed lines show the secondary sliding surfaces. (see text for discussion).

Using REFLEXW radar data processing software, the radar waves amplitude values of all the data acquisition track points in the profile at different depths can be extracted. In order to better understand the changes in the reflected radar wave intensity, we plotted the radar-wave amplitude curves for positions A, B, ZK2, C, D, E, ZK1, F and G (as depicted in **Figure 15**) on

http://dx.doi.org/10.5772/63068

the survey line I–I′ (**Figure 16**). Greater reflected radar wave intensity is indicated by a higher radar-wave amplitude value [41,43]. As shown in **Figure 16**, most curves showed relatively large amplitudes in the depth range of 0–2.5 m as the surface soil body is quite loose at this depth. At position A, the radar-wave amplitude increased substantially and abruptly at a depth of 4.5 m. We can conclude that the soil moisture content was relatively high at this position based on the characteristic differences between different types of soil bodies with regard to their radar-wave reflection [41,43]. We can therefore deduce the location of the sliding surface of the landslide mass. Likewise, an abrupt increase in radar-wave amplitudes occurred at

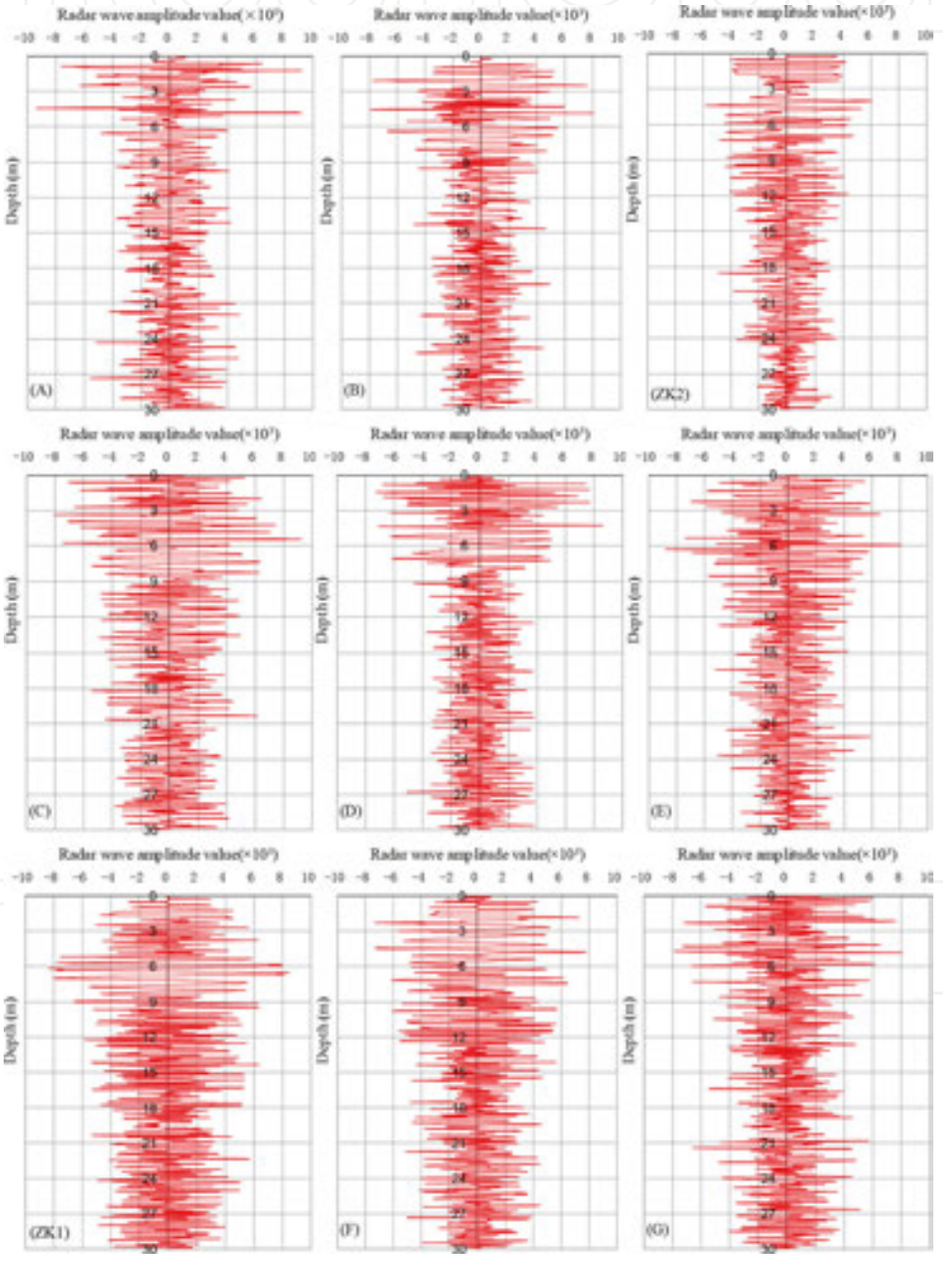

Figure 16. The radar-wave amplitude curves on the survey line I–I′. Positions A, B, ZK2, C, D, E, ZK1, F and G are all on the survey line I–I′ (as shown in Figure 15).

depths of 4.7 m, 4.7 m, 5.5 m, 5.5 m, 6.7 m, 6.5 m, 5.6 m and 5 m on line I–I′ at positions B, ZK2, C, D, E, ZK1, F and G, respectively, and the position of the sliding surface can be inferred. This is very close to the position of the sliding surface as denoted by thick the red line in **Figure 16**.

5.2. Survey line II–II′

The GPR profile recorded for survey line II–II′ is presented in **Figure 17**. The dotted red line is the low-frequency high-amplitude sync-phase axis, and we conclude that this represents the profile's sliding surface. This axis illustrates the landslide mass development depth range.

Using REFLEXW radar data processing software, we can obtain the radar-wave amplitude curves at positions A, B, C, D, ZK1, E, F, G and H (as shown in **Figure 17**) on the survey line II–II′, as shown in **Figure 18**. As can be seen from **Figure 18**, because the surface soil body is rather loose in this area, most curves showed relatively large amplitudes in the depth range of 0–2.5 m. D, ZK1 and E are all on the landslide mass, in positions D, ZK1 and E, a sudden and substantial increase in the radar-wave amplitude occurred at depths of 3.5 m, 6.5 m and 3.2 m, respectively, exhibiting abrupt changes. According to the differences in characteristic radar-wave reflection for different classes of soil bodies [41, 43], we inferred a relatively high soil moisture content at this location. This also implies the location of the landslide sliding surface. The deduced position of the sliding surface is about the same as that denoted by the red dashed line in **Figure 17**. Positions A, B, G and H were all located outside of the landslide mass. Except in the surface layer, i.e., in the depth range of 0–2.5 m, there were abrupt changes in the radar-wave amplitudes; at deeper depths, no abrupt changes were observed in the radar-wave amplitude curves.

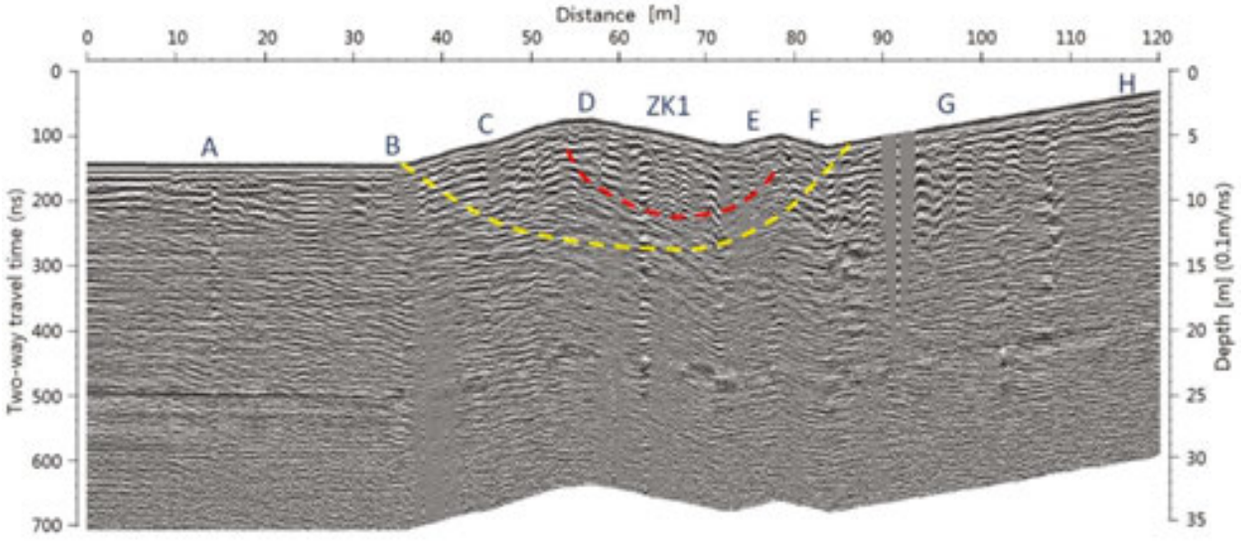

Figure 17. The GPR profile of the survey line II–II′. GPR detection date is on October 1, 2013. The red dashed line shows the current sliding surface. The yellow dashed line shows the position of the sliding surface for the paleo-landslide.

http://dx.doi.org/10.5772/63068

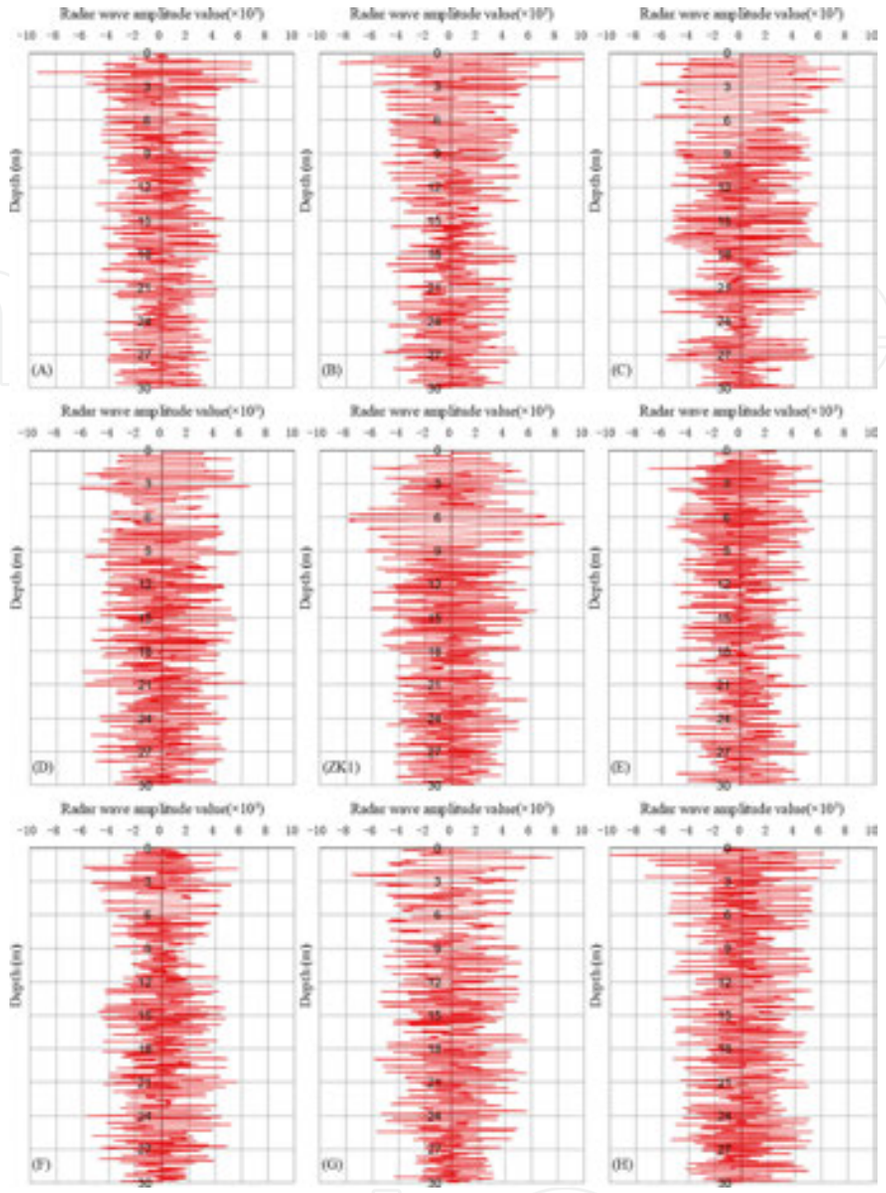

Figure 18. The radar-wave amplitude curves on the survey line II–II′. Positions A, B, C, D, ZK1, E, F, G and H are all on the survey line II–II′ (as shown in **Figure 17**).

As shown in **Figure 18**, in positions C, D, ZK1, E and F, the amplitude values showed substantial increases at depths of 6 m, 9.5 m, 9 m, 7 m and 3.5 m, respectively, exhibiting abrupt changes. These locations can be utilized to infer the sliding surface location of the paleolandslide (illustrated in **Figure 17** with yellow dashed lines). Meanwhile, the magnitude of the sudden alteration in the radar-wave amplitudes at the sliding surface location of the paleolandslide was less than the magnitude at the current sliding surface location.

The results of the GPR indicate relatively high soil moisture content at the sliding surface of the landslide mass. The drilling data also indicate very high moisture content of the sliding surface in the study area. These drilling results are in complete agreement with the results obtained from the HDR profile and the GPR profile.

6. Underlying mechanism of landslide development

A geological survey of the study area in May 2010 revealed permafrost in the shaded slopes on the two sides of the landslide [40]. Permafrost locations were identified by drilling into the profile of the survey line III–III′ (**Figure 19**). The HDR method was also used on June 2, 2010 for prospecting along survey line III–III′. Permafrost layer range in the profile of the survey line III–III′ can be inferred based on soil resistivity characteristics (in [41]). **Figure 20** presents the apparent electrical resistivity profile of survey line III–III′ collected in June 2, 2010 (as shown by the black dotted line).

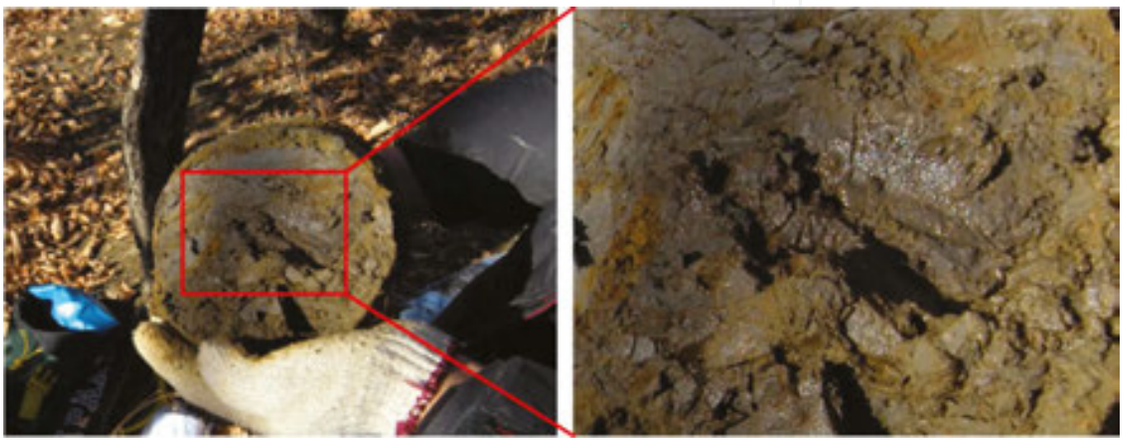

Figure 19. The photo of high temperature permafrost. Sampling location is in the survey line III–III′, at 40 m position on the *X* axis, the drilling time is in May 2010.

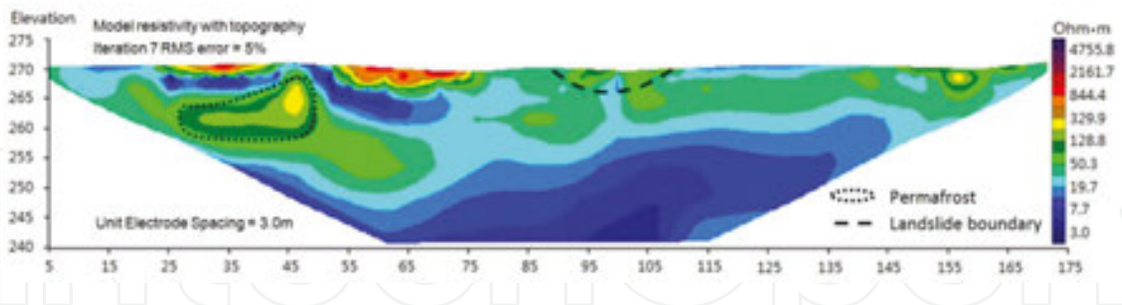

Figure 20. The electrical resistivity profile of the survey line III–III′ (2010-6-2).

Due to permafrost melting and concentrated summer rainfall, the landslide mass started to slip near the end of July in 2010 [40]. Borehole drilling and site survey data establish Landslide K178 + 530 as a shallow creeping consequent landslide. Water infiltration generated from concentrated summer precipitation in conjunction with water seepage produced from permafrost melting increase the local moisture content within the soil of hillsides. In the northwest section of the Lesser Khingan Range in China, this is the main cause of landslide formation. During the rainy season and the spring melting season, instability can easily occur. The relatively high number of bulging cracks on the landslide mass facilitates the infiltration

http://dx.doi.org/10.5772/63068

and accumulation of water. The highly permeable surface soil, sand and gravel layer, and the silty clay with a weathered sand interlayer produce an expedient route for water infiltration. The mudstone and siltstone layers beneath exhibit low permeability and produce watertight layers. Water generated from melting snow, precipitation, and permafrost melting is hindered by the impermeable layer during its downward infiltration, and the local moisture content sharply increases. Water therefore infiltrates along the interface of the permeable layer and the impermeable layer. This generates a slip zone. Combining the geophysical and drilling data, the position of the sliding surface can be determined, as shown by the red line in **Figure 21**.

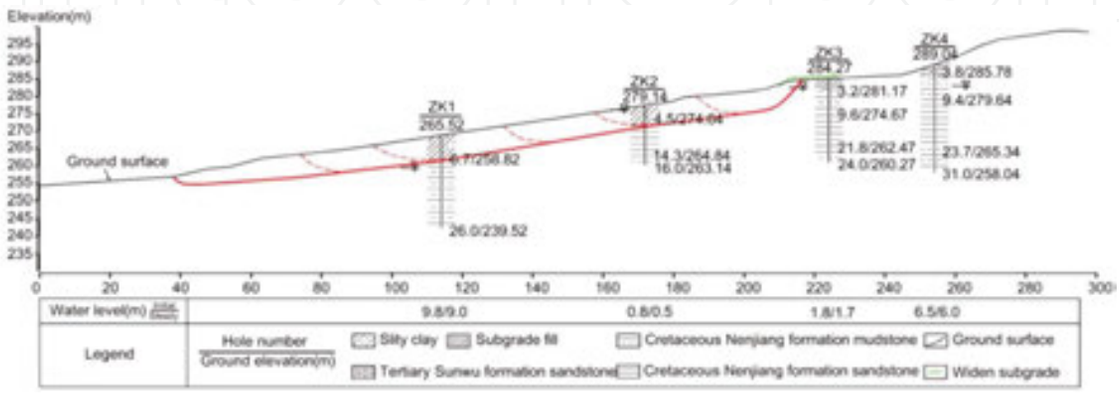

Figure 21. The stratigraphic distribution of section K178 + 530 (the thick red dashed line shows the position of the major sliding surface, the thin red dashed lines show the secondary sliding surfaces).

7. Landslide movement monitoring

Comprehensive examination and dynamic monitoring of the slip movement were performed for a representative landslide that could threaten the roadbed. This was done on the basis of geological survey and topographic measurements of the study area with the aim of investigating the impact of permafrost thaw on landslide movement.

Landslide K178 + 530 on the Bei'an-Heihe Highway (**Figure 6C**) is among the closest landslides to the roadbed and exhibits the most rapid slip rate. Due to the unavailability of monitoring and survey data prior to 2009, we could not determine the date of the initial slip. A satellite photo taken on June 15, 2004 indicates a straight-line distance of 101.26 m between the trailing edge and the leading edge of the landslide mass (**Figure 5B**). A satellite photo taken on September 12, 2010 indicates that the straight-line distance between the trailing and leading edges had increased to 145.05 m (**Figure 5C**). During this six year period, there was 43.79 m of movement in the leading edge of the landslide, whereas there was basically no movement in the position of the trailing edge.

Figure 22 presents the locations of the geophysical measurement lines, the drilling points, and monitoring points for ground temperature, displacement, and pore water pressure. The points ZK1, ZK2, ZK3, ZK4, E, and F in the figure denote the positions of the drilling, and lines I and

III denote the high-density resistivity measurement line and the ground-penetrating radar (GPR) measurement line, respectively. During the drilling in holes E and F, permafrost was found at a depth 2.2 m below the ground surface, and the permafrost thicknesses at points E and F were 3.7 m and 2.4m, respectively. The area of permafrost distribution in **Figure 22** is inferred according to **Figure 3**.

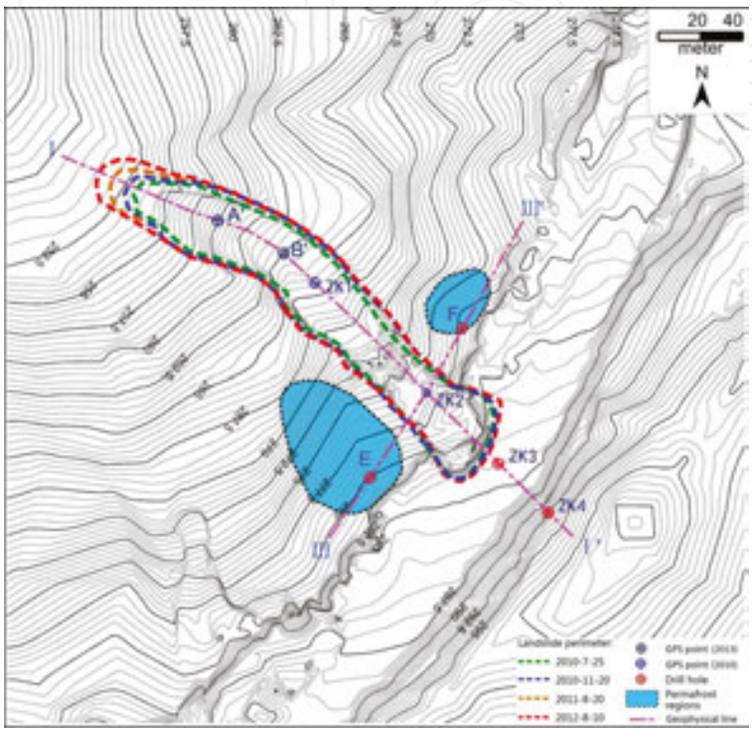

Figure 22. Distribution of the drillings, the geophysical measurement lines and points for monitoring displacement, ground temperature, and pore water pressure in Landslide K178 + 530.

Through drilling, GPR, and high-density resistivity prospecting; the profiles of Landslide K178 + 530 in cross section H along the sliding direction and in cross section G perpendicular to the slide direction were obtained (**Figures 23** and **24**).

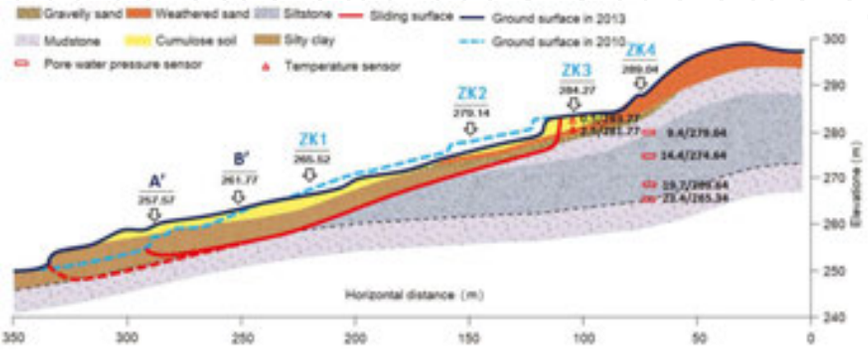

Figure 23. The profiles of Landslide K178 + 530 along the sliding direction.

http://dx.doi.org/10.5772/63068

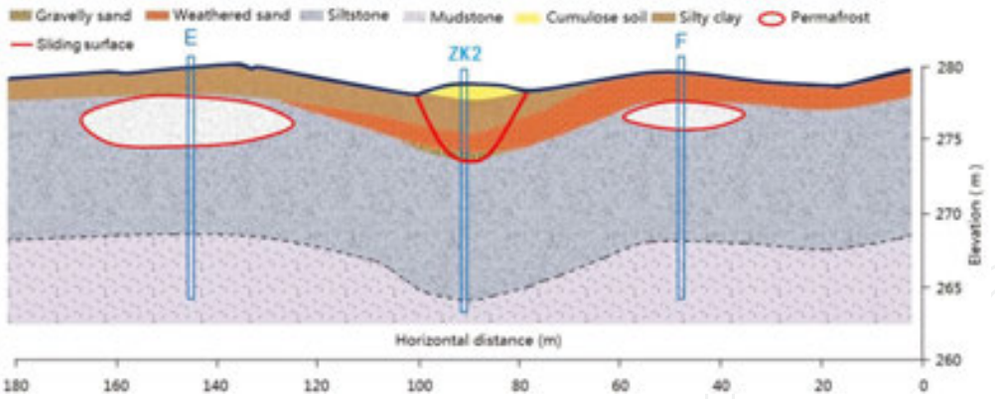

Figure 24. The profiles of Landslide K178 + 530 perpendicular to the slide direction.

In the boreholes ZK1 and ZK2 (**Figure 22**), we buried plastic displacement measurement piles that were 400 cm long with an above-ground height of 30 cm, The top of the pile was utilized to quantify the landslide mass slope displacement. ZK3 was used as the monitoring point for the ground temperature. Thermistor soil temperature sensors were set up at 0.5 m intervals from 0.5 m to 2.5 m below the ground surface. ZK4 served as the monitoring point of pore water pressure; in the borehole, steel-wire soil pore water pressure sensors were set up at 3.8 m, 9.4 m, 19.4 m, and 23.7 m depth. The relevant parameters were regularly monitored starting in July 2010.

We utilized a Real Time Kinematic-Global Positioning System (RTK-GPS) to monitor the movement of data collection points on the landslide surface. Point ZK1 horizontally slid by 69.03 m from July 2010 to August 2014, and its elevation decreased by 7.95 m. Point ZK2 horizontally slid by 113.97 m, and its elevation decreased by 17.37 m. From these values, we conclude that the angle between the horizontal plane and the slope dropped from 8.07° to 6.02°. Points A′ and B′ in **Figures 22** and **23** illustrate the locations of points ZK1 and ZK2 after sliding, respectively. These positions reflect data collected in August 2014.

Figure 25 illustrates the daily average atmospheric precipitation and ground temperature at point ZK3 on Landslide K178 + 530 at depths of 0.5 m and 2.0 m. The ground temperature data represents monitoring data collected in the study area. The daily average atmospheric precipitation and temperature represent the meteorological data collected via the Sunwu County weather station.

To facilitate the analysis of data, we defined the soil freeze period as the period from the time when the thermistor sensor at 0.5 m below ground surface detected temperature below 0°C in the autumn to the time when the thermistor sensor at 2.0 m below ground surface detected temperature changing from below to above zero degree Celsius in the spring. This period is displayed in light blue in **Figure 25**. We calculated the cumulative atmospheric precipitation for soil non-freeze and freeze periods, and these are illustrated in **Figure 23** via the dark blue bars. During the frozen soil period, snowmelt water and atmospheric precipitation cannot typically infiltrate to deep soil layers due to the seasonal frozen soil layer and **Figure 26** illustrates the pore water pressure recorded 19.4 m below the ground surface at point ZK4. At

the time of drilling, water was first observed for point ZK4 at a depth of 3.8 m. However, the stable water level recorded during the study period was within the range of 15.8–16.6 m. Unsaturated soil was recorded at 3.8 m and 9.4 m below the ground surface during the study period. Measurements from the pore water pressure sensor placed at a 23.7 m depth were unstable near the end of the study period. Data collected from the sensor placed at 19.4 m depth were therefore utilized to reflect pore water pressure at point ZK4.

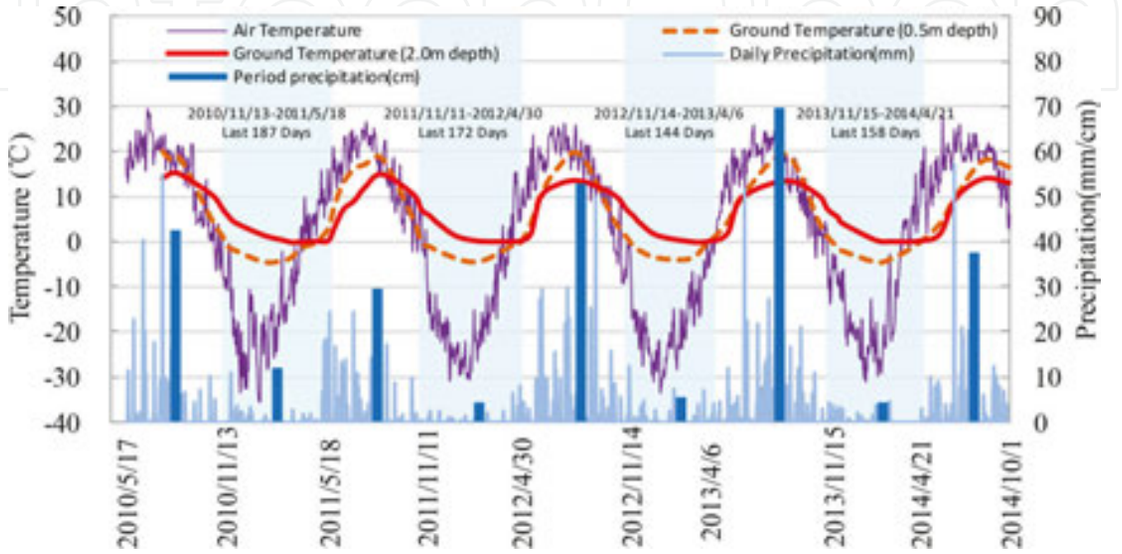

Figure 25. Daily average air temperature/precipitation/soil temperature in the depth of 50 cm, 200 cm in K178 + 530 section of Bei'an-Heihe Highway.

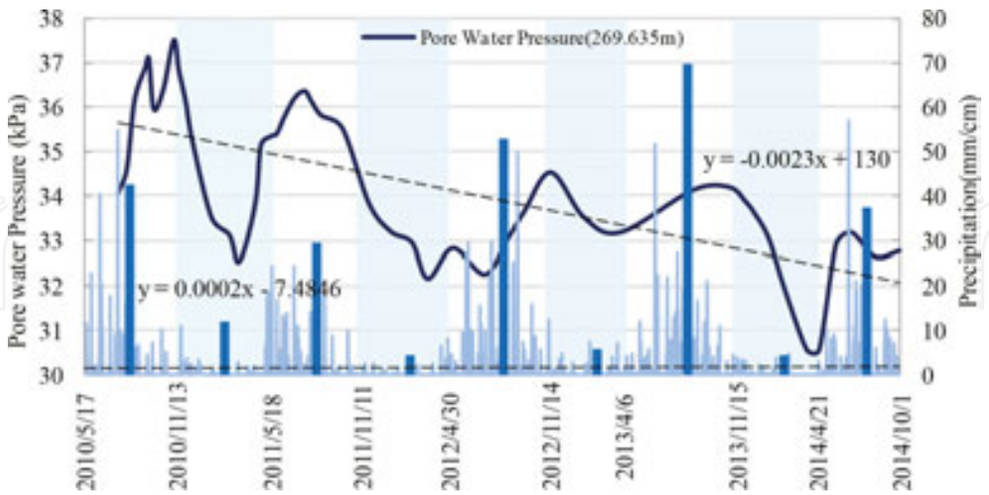

Figure 26. Daily precipitation and pore water pressure in the depth of 19.4 cm of ZK4 point in K178 + 530 section of Bei'an-Heihe Highway.

Figure 27 shows the displacement rates at point ZK1 and point ZK2 as well as the pore water pressure at point ZK4 over time. Displacement values collected via the RTK-GPS real-time

http://dx.doi.org/10.5772/63068

dynamic deformation monitoring system were divided by the time interval to obtain displacement rates.

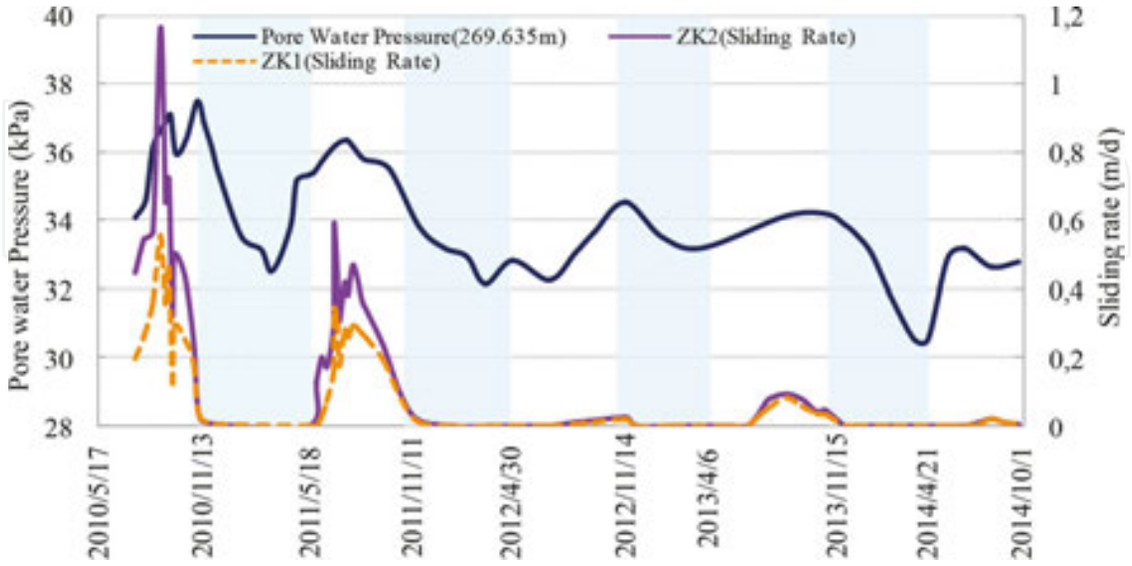

Figure 27. Horizontal displacement rates at point ZK1 and point ZK2 on the landslide mass and pore water pressure at point ZK4 (19.4 m depth) in K178 + 530 section of Bei'an-Heihe Highway.

8. Results, analysis, and discussion of data

The permafrost distribution determined by the present study is consistent with previous investigations [44, 45]. In the current study, we analyzed meteorological data from Sunwu County (collected 30 km to the south from the study area) to examine the climate change. The causes of landslide in the study area were evaluated preliminarily by means of permafrost distribution, geological survey of the study area, and topography. The roadbed instability that occurred during August 2000 in the section K176 + 900 to 178 + 200 of the Bei'an-Heihe secondary road was used as a case study.

The meteorological data from Sunwu County indicate that the variation in atmospheric precipitation was 8.93% during the 60 year period from 1954 to 2013. In the study area, this variation had a negligible long-term impact on the thermal state of the soil. As depicted in **Figure 2**, the increase in the average annual maximum temperature was substantially lower than the increase in the average annual minimum temperature. This indicates that the primary cause of the temperature increase was due to a reduction in the soil heat demand from the atmosphere and a rise in the soil's ability to radiate heat rather than an increase in the amount of direct radiation [46]. The latent heat of permafrost thaw caused the difference in the amplitude of temperature rise between the average annual minimum temperature and the average annual maximum temperature. The fact that these amplitudes differed by 47.05% over a 60 year period indicates rapid degeneration of the permafrost in the study.

Permafrost is not found in the section K176 + 900 to 178 + 200 (where overall roadbed instability occurred) of the previous Bei'an-Heihe secondary road (**Figure 3**). This is because the roadbed instability occurred in August 2000, while the ground temperature data used for **Figure 3** represent e ETM+ data collected by Landsat7 in 2009. The permafrost in this road section had entirely degraded entirely after nine years. In **Figure 3**, there are permafrost areas along the road on both sides of point ZK2, i.e., the right side of the K178 + 530 road section. However, no permafrost was found in borehole ZK2. Additionally, no aberrant data was detected below point ZK2 within 15 m along line III via the GPR and high-density resistivity methods. This suggests the absence of permafrost. This could be due to severe degradation of permafrost at this location was at a stage of severe degradation. In other words, the phase transition of soil moisture had already occurred with the associated transition to warm permafrost or melting permafrost. It could also be associated with the resolution of the ETM+ data from the Landsat7 satellite.

Figure 25 shows the relatively concentrated time period of the initial soil freezing in the study area. This typically fell in within 11 November to 15 November. However, the thawing period required for seasonal frost exhibited large annual variations at the same measurement point. This could be related to the level of winter snowfall and autumn precipitation in the previous year. It could also be related to the soil water thermal condition proximate to the maximum seasonal frost depth. However, these potential relationships require further investigation.

As shown in **Figure 26**, the pore water pressure at point ZK4 exhibited annual periodic changes. The pore water pressure began to increase in the spring of each year, reached the maximum value in the summer, and then subsequently decreased. At an interannual time scale, there was an overall downward trend in pore water pressure. This trend exhibited no correlation with atmospheric precipitation. Linear analysis indicates that the atmospheric precipitation in the study area rose by 0.318 mm during the study period, however, the pore water pressure at point ZK4 declined by 3.675 kPa. This resulted in a 36.75 cm decrease in its groundwater level. The groundwater reduction level was 1155 times the rise in atmospheric precipitation for the same period.

The slip rates measured at points ZK1 and ZK2 agree well with the pore water pressure results from point ZK4. During the study period, the landslide mass began to slip with thawing of seasonal frost and snowmelt each spring due to the gradual increase in the pore water pressure of the soil. The pore water pressure reached annual the peak during the concentrated rainfall of the summer, and the slip rate of the landslide obtained its maximum value at the same time. The soil pore water pressure gradually decreased with the landslide movement, and the sliding of the slope gradually stalled. The landslide movement exhibited notable seasonal activity and annual periodicity.

Figures 23 and **27** illustrate consistent trends in the slip rates of points ZK1 and ZK2 on the landslide mass. The displacement of point ZK2 was 1.65 times the movement at point ZK1 during the monitoring period. We conjecture that the displacement at point ZK1 might be due to force coming from the rear area of the landslide mass. For the period of 2010–2014 the annual maxima of pore water pressures at point ZK4 were 37.52 kPa, 36.37 kPa, 34.53 kPa, 34.14 kPa, and 33.19 kPa, respectively. The maxima decline each year, and the decline in amplitude was

http://dx.doi.org/10.5772/63068

relatively large in 2012. The maximum slip rates of point ZK2 from 2010 to 2014 were 115.7 cm/d, 59 cm/d, 2.55 cm/d, 9.63 cm/d, and 2.2 cm/d, respectively. Rapid sliding primarily occurred in the summer of 2011 and in 2010. There were decreases in the slip rate each year, and the largest reduction occurred in 2012. However, there was a slight rise in the slip rate in the summer of 2013. The underlying cause of these phenomena may be related to thawing permafrost which supplemented water to the landslide mass at points E and F (**Figure 22**), which are exterior to the lateral edge of the slope at point ZK2. Additionally, these phenomena could be related to the level of summer precipitation. As shown in **Figure 26**, the summer atmospheric precipitation in 2013 reached the largest value for the entire monitoring period (672 mm). This level was 14.33 mm higher than the second largest summer precipitation (which occurred in 2012) and it was 1.46 times the average summer atmospheric precipitation for the entire monitoring period. We therefore concluded that the slip rate of Landslide K178 + 530 during the monitoring period was mainly impacted by pore water pressure at the trailing edge of the landslide mass. At the same time, the slip rate was also impacted by the level of summer precipitation. Furthermore, the thawing of permafrost at the lateral edge of the slope was related to the pore water pressure at the trailing edge of the landslide mass. As permafrost thawed each year, its volume was reduced. This trend gradually decreased the pore water pressure at the trailing edge of the slope. Consequently, there were gradual decreases in the slip rate of the landslide mass each year.

9. Conclusion

In this study, we performed a comprehensive analysis via data on the study area climate as well as ground temperature, displacement, and pore water pressure data that were collected at transect points along Landslide K178 + 530 on the Bei'an-Heihe Highway. We arrived at the following main conclusions based on this analysis:

The northwest section of China's Lesser Khingan Range is positioned along the southern boundary of the high-latitude permafrost region. This area has been subject to temperature increases due to global climate change. The increase in yearly average minimum temperature is 3.45 times the increase in the average yearly maximum temperature. Permafrost degradation in the region is quite significant. There will be additional temperature increases in this region due to permafrost degradation. These patterns will also result in an acceleration of the northward migration of the southern boundary of the permafrost region.

Permafrost thaw results in increases in the number of landslides in the northwest section of China's Lesser Khingan Range. This subsequently results in regional topographical changes. Anthropogenic activity can accelerate the thawing of permafrost.

Infiltration of concentrated summer precipitation and water seepage from thawing permafrost both increase the moisture content in the soil of local hillsides. In the northwest section of the Lesser Khingan Range in China, this is the main casual factor for landslides.

Landslide movement in the northwest section of China's Lesser Khingan Range begins in the summer season with concentrated precipitation. The movement gradually stops when the soil freezes in the autumn. The landslide movement exhibits clear seasonal and annual periodicity.

The thawing process of permafrost on and near the landslide mass control the landslide slip rate and movement process in the northwest area of the Lesser Khingan Range. As the permafrost thaws each year and the volume is correspondingly reduced, there is an associated decrease in its ability to supplement water to the landslide mass. This results in a decrease in the landslide slip rate each year until it reaches zero. The landslides then tend towards stability.

The soil resistivity values above and below the sliding surface of the landslide mass are clearly different and exhibit an abrupt stratification. There is apparent resistivity layering at the position of the sliding surface in the landslide mass, the resistivity value decreased suddenly. In the profile of the GPR, the sliding surface is expressed as a low-frequency high-amplitude sync-phase axis, and there is an associated rapid rise in the radar wave amplitude. In practice, the abnormal abrupt changes in the GPR and HDR results can be used in this region to identify the sliding surface location of shallow landslides.

The results from the three methods we used to investigate landslides in the study area, i.e., HDR, GPR, and drilling, generally agree with regard to the sliding surface position. This indicates that the GPR and HDR methods are economical, rapid, and reliable methods for prospecting in landslide areas. These methods can be applied to shallow landslides in high-latitude permafrost regions for accurate and rapid identification of the sliding surface position. These techniques can also aid in the generation of accurate data for engineering projects to ensure that appropriate measures are adopted.

Acknowledgements

We thank the Science and Technology Project of the Chinese Ministry of Transport (2011318223630) and the International Landslide Research Program (IPL-167) for funding support. We are also grateful to an anonymous referee who helped improve the manuscript.

Author details

Wei Shan*, Ying Guo, Zhaoguang Hu, Chunjiao Wang and Chengcheng Zhang

*Address all correspondence to: shanwei456@163.com

Institute of Cold Regions Science and Engineering, Northeast Forestry University, Harbin, China

http://dx.doi.org/10.5772/63068

References

[1] Guo D X, Wang S L, Lu G, Dai J B, and Li E Y. Regionalization of permafrost in the Da and XiaoXing'anling Mountains in northeastern China. Journal of Glaciology and Geocryology. 1981; 3: 1–9.

[2] Zhou Y W, Wang Y X, Gao X W, and Yue H S. Ground temperature, permafrost distribution and climate warming in northeastern China. Journal of Glaclology and Gecryology. 1996; 18: 139–147.

[3] Sun G Y, Yu S P, and Wang H X. Causes south borderline and subareas of permafrost in Da Hinggan Mountains and Xiao Hinggan Mountains. Scientia Geographica Sinica. 2007; 27: 68–74.

[4] Jin H J, Li S X, Wang S L, and Zhao L. Impacts of climatic change on permafrost and cold regions environments in China. Acta Geographica Sinica. 2000; 55: 161–173.

[5] Wei Z, Jin H J, and Zhang J M. Prediction of permafrost changes in Northeastern China under a changing climate. Science China: Earth Sciences. 2010; 41: 74–84. DOI: 10.1007/s11430-010-4109-6.

[6] He R X, Jin H J, Lv L Z, Yu S P, Chang X L, Yang S Z, Wang S L, and Sun G Y. Recent changes of permafrost and cold regions environments in the northern part of Northeastern China. Journal of Glaciology and Geocryology. 2009; 31: 525–531.

[7] Solomon S, Qin D, and Manning M. Summary for policymakers. Climate Change 2007: The physical science basis (Contribution of Working Group I to the Fourth Assessment Report of the Intergovernmental Panel on Climate Change). Intergovernmental Panel on Climate Change. 2007 (www.ipcc.ch/).

[8] IPCC. Summary for policymakers. Working group I contribution to the IPCC fifth assessment report climate change 2013: the physical science basis. Cambridge, UK. Cambridge University Press; 2013.

[9] Ding Y H, Ren G Y, and Shi G. National assessment report of climate change (I): climate change in China and its future trend. Advances in Climate Change Research. 2006; 2: 3–8.

[10] Shi P J, Sun S, and Wang M. Climate change regionalization in China (1961-2010. Science China: Earth Sciences. 2014;44: 2294–2306. DOI: 10.1007/s11430-014-4889-1.

[11] Chang X L, Jin H J, Yu S P, Sun H B, He R X, Luo D L, Sun G Y, and Lu L Z. Influence of vegetation on frozen ground temperatures the forested area in the Da Xing'anling Mountains, Northeastern China. Acta Ecologica Sinica. 2011; 31: 5138–5147.

[12] Zhou Y W, and Guo D X. Principal characteristics of permafrost in China. Journal of Glaciology and Geocryology. 1982; 4: 1–19.

[13] Chang X L, Jin H J, and He R X. Review of permafrost monitoring in the northern Da Hinggan Mountains, Northeast China. Journal of Glaciology and Geocryology. 2013; 35: 93–100.

[14] Jin H J, Wang S L, and Lv L Z. Features of permafrost degradation in Hinggan Mountains, northeastern China. Scientia Geographica Sinica. 2009; 2: 223–228.

[15] Arndt D S, Blunden J, and Willett K. State of the Climate in 2011 Special Supplement to the Bulletin of the American Meteorological Society. Bulletin of the American Meteorological Society. 2012; 93(7).

[16] Eu-Fp7. A summary for policymakers. PD Investigación. ACQWA: Assessing Climate impacts on the Quantity and quality of Water. A large integrating project under EU Framework Programme 7 (FP7). 2008.

[17] Sassa K, Yin Y, and Canuti P. The Third World Landslide Forum, Beijing, 2014. Landslides. 2015; 12(1): 1–16 (http://iplhq.org/category/home/)

[18] Sassa K. ICL strategic plan 2012–2021—To create a safer geo-environment. Landslides. 2012; 9(2): 155–164 (http://iplhq.org/category/home/).

[19] Guo Y, Canuti P, Strom A, Hideaki M, and Shan W. The First Meeting of ICL Landslides in Cold Regions Network, Harbin, 2012. Landslides. 2013; 10: 99–102. DOI: 10.1007/s10346-012-0369-x.

[20] Shan W, Guo Y, Zhang C C, Hu Z G, Jiang H, and Wang C J. Climate-change impacts on embankments and slope stability in permafrost regions of Bei'an-Heihe Highway. Landslide Science for a Safer Geoenvironment. 2014; 1: 155–160. DOI: 10.1007/978-3-319-04999-1_18.

[21] Shan W, Guo Y, Wang F, Marui H, and Strom A. Landslides in cold regions in the context of climate change (Springer: Environmental Science and Engineering). ISBN 978-3-319-00866-0. ISBN 978-3-319-00867-7 (eBook). 2014;105–109. DOI: 10.1007/978-3-319-00867-7

[22] Grab S W, and Linde J H. Mapping exposure to snow in a developing African context: implications for human and livestock vulnerability in Lesotho. Natural Hazards. 2014; 71: 1537–1560. DOI: 10.1007/s11069-013-0964-8.

[23] Ballantyne C K, Sandeman G F, Stone J O, and Wilson P. Rock-slope failure following Late Pleistocene deglaciation on tectonically stable mountainous terrain. Quaternary Science Reviews. 2014; 86: 144–157.

[24] Nussbaumer S, Schaub Y, Huggel C, and Nat AW. Risk estimation for future glacier lake outburst floods based on local land-use changes. Hazards and Earth System Sciences. 2014; 14: 1611–1624. DOI: 10.5194/nhess-14-1611-2014.

[25] Haeberli W. Mountain permafrost – research frontiers and a special long-term challenge. Cold Regions Science and Technology. 2013; 96: 71–76.

[26] Kliem P, Buylaert J P, Hahn A, Mayrd C, Murray A S, Ohlendorf C, Wastegård S, Zolitschka B, and Team T P S. Magnitude geomorphologic response and climate links of lake level oscillations at Laguna Potrok Aike, Patagonian steppe. Quaternary Science Reviews. 2013; 71: 131–146.

[27] Fischer L, Hugge C, Kaab A, and Haeberli. Slope failures and erosion rates on a glacierized high-mountain face under climatic changes Earth Surf. Landforms. 2013; 38: 836–846. DOI:10.1002/esp.3355

[28] Starnberger R, Drescher S R, Reitner J M, Rodnight H, Reimer P J, and Spötl C. Late Pleistocene climate change and landscape dynamics in the Eastern Alps: the inner-alpine Unterangerberg record (Austria) Quaternary Science Reviews. 2013; 68, 17–42.

[29] Stoffel M, Tiranti D, and Huggel C. Climate change impacts on mass movements – case studies from the European Alps. Science of the Total Environment 2014; 22014: 1255–1266.

[30] Wang C J, Shan W, Guo Y, Hu Z G, and Jiang H. Permafrost Distribution Study Based on Landsat ETM+ Imagery of the Northwest Section of the Lesser Khingan Range. Landslide Science for a Safer Geoenvironment. 2014a; 3: 529–534. DOI: 10.1007/978-3-319-04996-0_81.

[31] He R X, Jin H J, Chang X L, Lv L Z, Yu S P, Yang S Z, Wang S L, and Sun G Y. Degradation of permafrost in the northern part of Northeastern China: Present state and causal analysis. Journal of Glaciology and Geocryology. 2009; 31: 829–834.

[32] Zhang Y, Wu Q B, and Liu J P. Distribution characteristics of the permafrost in the section from Heihe to Bei' an in the Xiao Hinggan Mountains. Journal of Glaciology and Geocryology. 2001;23:312–317.

[33] Wang B, Sheng Y, and Liu J P. Distribution and degradation of permafrost in Xiao Hinggan Mountains along the Heihe-Dalian Highway. Journal of Glaciology and Geocryology. 2001; 23: 302–306.

[34] Wang S H, Qi J L, Yin Z Y, Zhang J M, and Ma W. A simple rheological element based creep model for frozen soils. Cold Regions Science and Technology Cold Regions Science and Technology. 2014; 106: 47–54. DOI: 10.1016/j.coldregions.2014.06.007.

[35] Loke M H, and Barker R D. Rapid least-squares inversion of apparent resistivity pseudosections using a quasi-Newton method. Geophys Prospect. 1996; 44: 131–152.

[36] Tripp A C, Hohmann G W, and Swift C M. Two-dimensional resistivity inversion. Geophysics. 1984; 49: 1708–1717.

[37] Sasaki Y. Resolution of resistivity tomography inferred from numerical simulation. Geophys Prospect. 1992; 40: 453–463.

[38] Coggon J H. Electromagnetic and electrical modelling by the finite element method. Geophysics. 1971; 36: 132–155.

[39] Dey A, and Morrison H F. Resistivity modelling for arbitrarily shaped two-dimensional structures. Geophys Prospect. 1979; 27: 106–136

[40] Shan W, Hu ZG, Guo Y, Zhang C C, Wang C J, Jiang H, Liu Y, and Xiao J T. The impact of climate change on landslides in southeastern of high-latitude permafrost regions of China. Frontiers in Earth Science. 2015; 3(7): 1–11. doi: 10.3389/feart.2015.00007

[41] Telford W M, Geldart L P, and Sheriff R E. Applied geophysics. Geological Journal. 1992; 27(1): 97. DOI: 10.1002/gj.3350270119.

[42] Daniels D J. The Institution of Electrical Engineers, London, United Kingdom, editors. Ground Penetrating Radar. 2nd ed. London: IEE Radar; 2004.

[43] Benedetto A, Benedetto F, and Tosti F. GPR applications for geotechnical stability of transportation infrastructures. Nondestructive Testing and Evaluation. 2013; 27(3): 253–262.

[44] Wang C J, Shan W, Guo Y, Hu Z G, and Jiang H. Permafrost distribution study based on Landsat ETM+ Imagery of the northwest section of the lesser Khingan Range. Landslide Science for a Safer Geoenvironment. 2014; 3: 529–534. DOI: 10.1007/978-3-319-04996-0_81.

[45] Wang C J, Shan W, Guo Y, Hu Z G, and Jiang H. Permafrost distribution research based on remote sensing technology in northwest section of Lesser Khingan Range in China. Engineering Geology for Society and Territory. 2015; 1: 285–290. DOI: 10.1007/978-3-319-09300-0_53.

[46] Chen J, Sheng Y, and Cheng G D. Discussion on protection measures of permafrost under the action of engineering from the point of earth surface energy balance equation in Qinghai Tibetan Plateau. Journal of Glaciology and Geocryology. 2006; 28: 223–228.